

# Reshaping quantum device noise via quantum error correction

Yue Ma<sup>1</sup>, Michael Hanks<sup>1</sup>, Evdokia Gneusheva<sup>1</sup>, and M. S. Kim<sup>1</sup>  
<sup>1</sup>*Blackett Laboratory, Imperial College London,  
SW7 2AZ, United Kingdom*

We show that quantum error correction codes can reshape the native noise profiles of quantum devices, explicitly considering trapped-ion systems. We analytically derive the quantum channels describing noisy two-qubit entangling gates, showing that the leading error term is the sum of single-qubit bit-flip errors. This motivates our choice of compatible quantum error correction code – the bit-flip repetition code, based on which we add a parameterised single-qubit gate for extra tunability. We analytically derive the resulting logical quantum channel, illustrating the noise profile transformation. We then demonstrate the noise reshaping on the IonQ Aria-1 quantum hardware, where the data shows consistency with our analytical model. Our results represent first step towards using quantum error correction codes in genuine quantum ways, paving the way to exploiting the device native noise as features for open quantum dynamics simulations.

All quantum computers [1] face a significant practical obstacle – noise [2, 3]. The most promising route towards overcoming this obstacle is via quantum error correction [4–10]. It uses redundant qubits, such that part of the superposition is measured for gaining information about the error induced by the noise, while the other part that encodes the quantum information is effectively protected from the noise. Most investigations on quantum error correction assume Pauli errors [11, 12]. Although this assumption largely simplifies the studies of scalability [13] and threshold [14], it removes the features of the underlying physical systems. It remains unexplored how the combination of structured native noise and quantum error correction will lead to interesting device-specific applications in the current NISQ era, one of which is using device noise to assist simulations of open quantum dynamics. This application has been demonstrated in the context of quantum error mitigation [15, 16], but native noise structures were not involved.

Here we address the aforementioned challenge. We focus on the trapped-ion implementation of quantum computers, where the mediator for qubit-qubit interactions, the common vibrational mode, is also a quantum degree of freedom [17–19]. The two-qubit entangling gates, which are a source of seriously noisy quantum operations, have been experimentally characterised [20–22], but only in terms of the gate fidelity rather than the noise structure. On the other hand, the performance of quantum error correction codes in trapped-ion systems under phenomenological noise models has been simulated [23, 24], but the focus was only on the classical number of logical error rate. In this paper, we derive the noise structure of the two-qubit entangling gates, and show that compatible error correction codes, upon modifications for increased tunability, can reshape the native noise into logical quantum channels that have different noise structures. We then demonstrate our findings on the IonQ Aria-1 quantum device, where the data reasonably match our analytical results.

*Noisy Mølmer-Sørensen gates* — Mølmer-Sørensen gates [17, 18] implement the two-qubit entangling gates in trapped-ion based quantum devices. Qubits, realized via intrinsic spin states of the ions, effectively interact with each other via their common vibrational mode. The dominant noise for Mølmer-Sørensen gates has been pointed out to be from the motional dephasing [25], whose Lindblad form is  $C = \sqrt{\Gamma_P} a^\dagger a$ , with  $\Gamma_P$  the dephasing rate, and  $\hat{a}$  the annihilation operator for the vibrational mode. The dynamics can be analytically solved under some approximations, following the method of Ref. [17]. Specifically, the approximations are that in the interaction picture with respect to all the unitary dynamics, the state of the two qubits is always separable from the state of the vibrational mode, and the latter is kept in a thermal state with mean phonon number  $n_{\text{th}}$ . For the fully entangling gate which is equivalent to the CNOT gate up to single-qubit gates [17, 26, 27], we find that the canonical Kraus operators of the quantum channel that maps the target state to the state produced by the noisy gate have the following structure,

$$\begin{aligned} K_1 &= a_1 I + a_3 J_y^2, \\ K_2 &= k_2 J_y, \\ K_3 &= a_2 I + a_4 J_y^2, \end{aligned} \quad (1)$$

where the coefficients have closed form solutions (the derivations are presented in the Supplemental Material [28]), and the total angular momentum is  $J_y = (Y_1 + Y_2)/2$ , where  $Y_i$  are Pauli operators.

An example of how these coefficients change with the dephasing rate is shown in Fig. 1. We have chosen the parameters [17] according to the weak coupling regime that most experimental realizations of Mølmer-Sørensen gates follow [29–32]. Specifically, the Lamb-Dicke parameter is  $\eta = 0.1$ , the Rabi frequency is  $\Omega = 0.1$ ,  $n_{\text{th}} = 0.05$ , and  $K = 25$  is an integer describing the number of loops traversed in the phase space of the vibrational mode [19]. For comparison, in Fig. 1, we also show numerical simu-

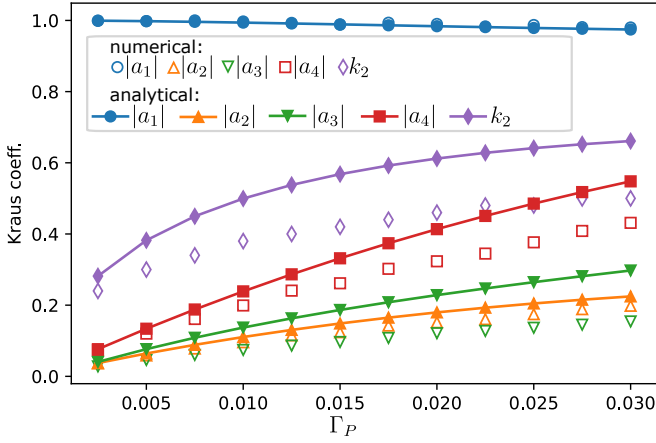


FIG. 1. Coefficients of the canonical Kraus operators in Eq. (1), as the value of  $\Gamma_P$  changes, comparing the analytical approximate solutions (solid line with solid markers) with the numerical exact solutions (open markers).

lation results obtained without the approximations mentioned above, where we find that the canonical Kraus operators are still in the form of Eq. (1), and the coefficients have only reasonably small deviations from the analytical ones. Importantly,  $K_2$  is the dominant error term. Here the Pauli Y operator originates from the conventional choice of basis in theoretical derivations [17], where the entangling gate is also defined in the  $y$ -basis. Experimentally the basis can be chosen at will. For the IonQ Aria-1 quantum device, the fully entangling gate is in the  $x$ -basis [27], therefore the dominant error in the noisy Mølmer-Sørensen gate is deduced to be  $X_1 + X_2$ , i.e., the sum of the bit-flip error for each qubit.

We will demonstrate reshaping this native device noise by quantum error correction codes. Its structure suggests that codes designed to correct single-qubit bit-flip error are the optimal choice, the simplest of which is the three qubit bit-flip repetition code as will be described below. Moreover, the error discretization by syndrome measurements [7] implies that this native noise will effectively act as single-qubit stochastic noise once incorporated into the code.

*Bit-flip repetition code* — The three-qubit bit-flip repetition code is the simplest quantum error correction code. Using three physical qubits to encode one logical qubit, it is designed to correct one bit-flip error.

Suppose that we want to store a physical state  $|\psi\rangle = \alpha|0\rangle + \beta|1\rangle$ , but the qubit has probability  $p$  of being subject to the bit-flip error described by the Pauli  $X$  operator. We can protect the quantum information from this error by encoding the state into a logical state  $|\bar{\psi}\rangle = \alpha|000\rangle + \beta|111\rangle$ . We perform syndrome measurements on the stabilizers ( $Z_1Z_2, Z_2Z_3$ ) and apply correction operators conditioning on the measurement results, as listed in Table I.

The probability of recovering the original state is

$Z_1Z_2$	$Z_2Z_3$	Correction
+1	+1	$I$
+1	-1	$X_3$
-1	+1	$X_1$
-1	-1	$X_2$

TABLE I. Syndrome measurements and the corresponding correction for the three-qubit bit-flip repetition code.

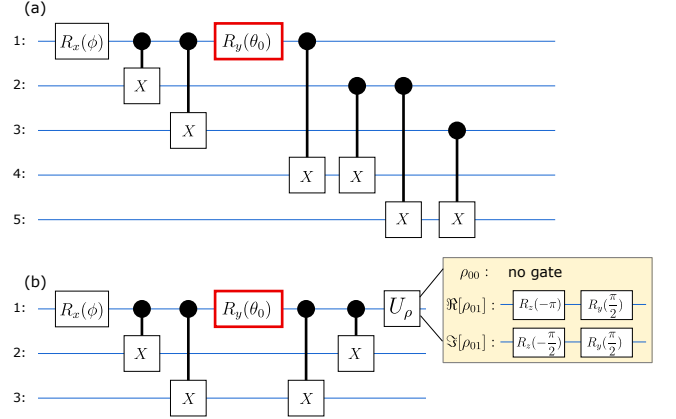


FIG. 2. Quantum circuits to implement the modified repetition code for noise reshaping. All qubits are measured at the end in the computational basis. The correction operators as listed in Table I are implemented via classical post-processing. (a) Two ancilla qubits are included for measuring  $\rho_{00}$  with reduced measurement errors. (b) Choosing three different  $U_\rho$  corresponds to measuring  $\rho_{00}$ ,  $\Re[\rho_{01}]$  or  $\Im[\rho_{01}]$ .

$\bar{p}_{\text{success}} = (1 - p)^3 + 3(1 - p)^2p$ , which is larger than the unencoded one  $p_{\text{success}} = 1 - p$  for  $p < 0.5$ . Therefore the effect of bit-flip errors is reduced.

We are interested in how the code reshapes the noise profile of quantum computers, rather than just using a classical number to access the success rate of error correction: The output logical state from the repetition code can be viewed as the initial logical state going through a quantum channel that is different from the one on the physical qubit level. To achieve extra tunability, we modify the code by inserting a parameterized single-qubit gate, which will be shown next.

*Reshaping the physical noise* — We have demonstrated that the bit-flip repetition code is able to change the error rate of the noise channel: The single-qubit bit-flip error with probability  $p$  is converted into the logical bit-flip error with probability  $\bar{p}_{\text{success}}$ . We can reshape the structure of the noise channel as well, if we allow modifications to the code. One of the simplest options is to add a unitary gate associated with rotation around the  $y$ -axis [33],

$$R_y(\theta_0) = \begin{pmatrix} \cos(\theta_0/2) & -\sin(\theta_0/2) \\ \sin(\theta_0/2) & \cos(\theta_0/2) \end{pmatrix}, \quad 0 \leq \theta_0 \leq \pi, \quad (2)$$

on physical qubit 1, after the physical bit-flip noise chan-

nels have been applied and before the syndrome measurements. After nontrivially keeping track of how syndrome measurements and corrections act on the logical states, we find that, the resulting output state is expressed as the initial logical state  $|\psi\rangle$  going through a quantum channel described by the following Kraus operators,

$$\begin{aligned} K_I &= (1-p)\sqrt{1+2p}\cos(\theta_0/2)I_L, \\ K_X &= \sqrt{3p^2-2p^3}\cos(\theta_0/2)X_L, \\ K_Y &= \sqrt{2p-3p^2+2p^3}\sin(\theta_0/2)Y_L, \\ K_Z &= \sqrt{1-2p+3p^2-2p^3}\sin(\theta_0/2)Z_L, \end{aligned} \quad (3)$$

where  $I_L = I_1I_2I_3$  is the logical identity operator,  $X_L = X_1X_2X_3$ ,  $Z_L = Z_1$  and  $Y_L = -iZ_LX_L$  are the logical Pauli- $X$ ,  $Z$  and  $Y$  operators, respectively. This is our core analytical result of reshaping noise via quantum error correction. Compared with the physical bit-flip channel, this channel has reduced  $X$  error, but has  $Y$  and  $Z$  errors that are not present on the physical qubit level. The correlations between the weights of the errors are also nontrivial (see the Supplemental Material [28] for details). Moreover, the tunability of the channel upon changing  $\theta_0$  relies on the non-zero bit-flip rate  $p$ : We are exploiting the noise as a useful feature to unveil the abundant structures of the reshaped channel.

The analysis above theoretically demonstrates the principle of noise reshaping via quantum error correction. To implement it, the encoding, syndrome measurements and corrections need to be done through quantum circuits. Moreover, the native noise comes from imperfect operations in the quantum circuits. These will be introduced next.

*The quantum circuits* — Two of the simplest quantum circuits for noise reshaping via the modified three-qubit bit-flip repetition code are shown in Fig. 2. The  $R_x(\phi)$  gate initializes the physical state  $|\psi\rangle$  with  $\alpha = \cos(\phi/2)$  and  $\beta = -i\sin(\phi/2)$ . More quantum gates can be included for initialization to more general quantum states. The subsequent two CNOT gates encode the physical state into the logical state  $|\psi\rangle$ . On real quantum devices, these two-qubit entangling gates are noisier than single-qubit gates. We thus exploit the native noise structure to be reshaped by the circuits. For trapped-ion-based quantum devices, the CNOT gate is compiled into the Mølmer-Sørensen gate (see the Supplemental Material [28], where all the conventions are also clarified), whose leading error is the sum of bit-flip errors, as shown in Eq. (1) and Fig. 1. Upon error discretization by syndrome measurements [7], the native noise becomes compatible with the bit-flip error considered in Eq. (3). We further make the error rate tunable by repeatedly inserting [20, 21] different numbers of redundant pairs of Mølmer-Sørensen gates that correspond to the identity operator in the noiseless case. These arrangements make our approach unique: We neither rely on randomization

techniques [11] that are commonly used in literature for trivialising the device noise, nor artificially introduce bit-flip errors for each physical qubit.

The next  $R_y(\theta_0)$  gate corresponds to the code modification as in Eq. (2). The rest of the circuits are tailored to reconstruct the output logical state,  $\langle 000|\bar{\rho}_f|000\rangle \equiv \rho_{00}$  and  $\langle 000|\bar{\rho}_f|111\rangle \equiv \rho_{01}$ . Syndrome measurements and corrections are included in this part of the circuits. Considering the practicality of quantum devices, we do not explicitly apply mid-circuit measurements or multi-qubit operators. Instead we measure all qubits in the computational basis at the end of the circuits and perform classical post-processing. The circuit in Fig. 2(a) explicitly uses two ancilla qubits (labelled 4 and 5) to compensate for measurement errors: Only results that are compatible with the code space basis  $\{|000\rangle_{123}, |111\rangle_{123}\}$  are counted in the statistics. The circuit in Fig. 2(b) does not include ancilla, but is able to estimate both  $\rho_{00}$  and the complex-valued  $\rho_{01}$  once the corresponding single-qubit gate  $U_\rho$  is selected at the end. More technical details are included in the Supplemental Material [28].

For running on a quantum device, the circuits in Fig. 2 need to be compiled into the native gates of the device. We have chosen one trapped-ion-based device – IonQ Aria-1. We will next present the hardware results and show their consistency with our analytical model of noise reshaping, Eq. (3).

*IonQ Aria-1 results* — We compile the quantum circuits in Fig. 2 into sequences of IonQ Aria-1 native gates, where in particular two-qubit entanglements are generated by Mølmer-Sørensen gates. Technical details are in the Supplemental Material [28].

The results obtained from the quantum device, for using the circuit Fig. 2(a) to estimate  $\rho_{00}$ , are shown as the data points in Fig. 3(a). Without any redundant pair of Mølmer-Sørensen gates (blue up-pointing triangles), the dependence of  $\rho_{00}$  on  $\theta_0$  is very weak and not resolvable. Once we add a small number of redundant pairs (orange circles, green down-pointing triangles, red squares, corresponding to 5, 7 and 10 repetitions respectively), the dependence of  $\rho_{00}$  on  $\theta_0$  becomes clearly visible:  $\rho_{00}$  decreases as  $\theta_0$  increases from 0 to  $\pi$ . This feature is made available by the existence of the device noise. In addition, we can also resolve the decrease of  $\rho_{00}$  as the number of redundant pairs increase. It means that the  $\rho_{00} - \theta_0$  curves for different numbers of repetitions are well-separated and clearly resolvable. If we add a very large number of redundant pairs (purple right-pointing triangles, brown diamonds, corresponding to 15 and 25 repetitions respectively), the dependence of  $\rho_{00}$  on  $\theta_0$  and the number of repetitions becomes less clear. For 15 repetitions,  $\rho_{00}$  increases with  $\theta_0$ , while for 25 repetitions,  $\rho_{00}$  decreases with  $\theta_0$  slightly. Except the case of 25 repetitions, the data match quantitatively well with the model Eq. (3), as plotted as lines in Fig. 3(a). We have manually chosen the best values of  $p$  to fit the

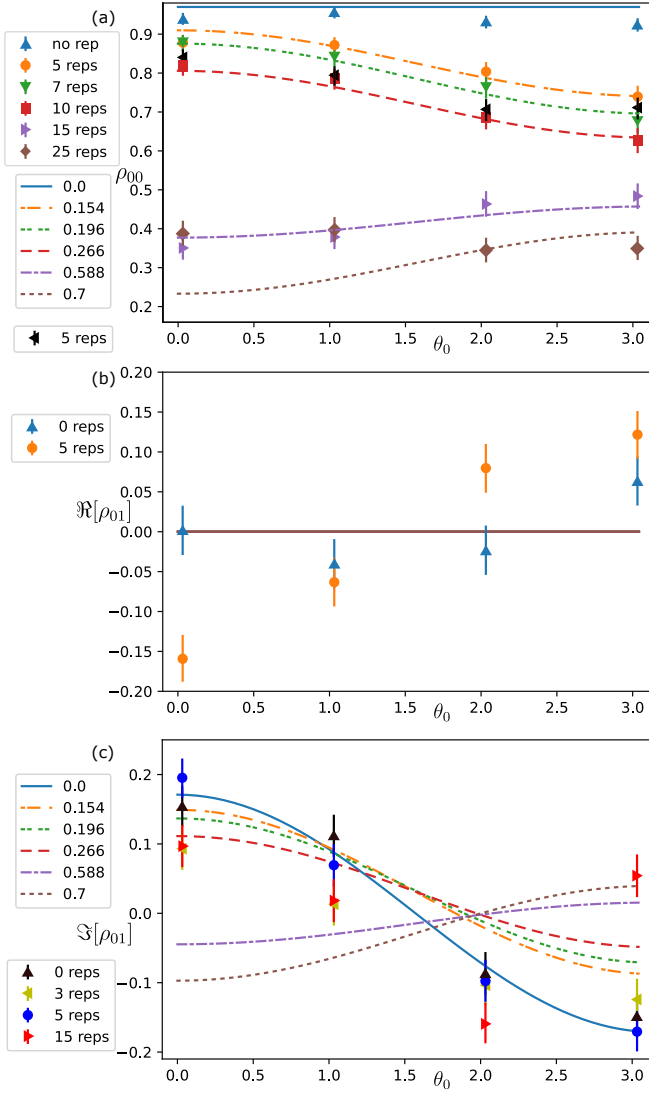


FIG. 3. Measurement results obtained from the IonQ Aria-1 quantum device (data points), in comparison with the model Eq. (3) (lines). Each data point is averaged over 1000 shots. Error bars are 95% confidence intervals computed from the Wilson score [34]. The number of repetitions refers to the number of the inserted pairs of redundant Mølmer-Sørensen gates after each encoding gate. For the lines, each bit-flip rate  $p$  is an integer multiple of the Mølmer-Sørensen gate infidelity, 0.014 at the time of measurements. (a) The diagonal element of the output logical density matrix,  $\rho_{00}$ . The data come from the compiled version of Fig. 2(a), except the black left-pointing triangles which are from the compiled circuit of Fig. 2(b) for reference (see the main text for details). (b){c}) The real {imaginary} part of the off-diagonal element  $\rho_{01}$ . The data come from the compiled circuit of Fig. 2(b).

data, under the constraint that  $p$  are integer multiples of the Mølmer-Sørensen gate infidelity. In the Supplemental Material [28], we also compare the hardware data with the simulation results of compiled quantum circuits under various noise models.

The results from the circuits in Fig. 2(b), which recon-

struct  $\rho_{00}$ ,  $\Re[\rho_{01}]$  or  $\Im[\rho_{01}]$  without using ancilla qubits, are included in Fig. 2(a-c). In Fig. 3(a), the black data points (left-pointing triangles) are based on the compiled version of Fig. 2(b) for 5 repetitions. The smaller  $\rho_{00}$  compared with the orange circles for each  $\theta_0$  results from the lack of post-selection for compensating measurement errors as there is no ancilla qubit. In Fig. 3(b), we compare the data for  $\Re[\rho_{01}]$  with the model Eq. (3) which predicts  $\Re[\rho_{01}] = 0$  for all  $\theta_0$  and  $p$ . The data indeed show small values of  $\Re[\rho_{01}]$  around 0. The deviations from 0 can be associated with noise sources other than the Mølmer-Sørensen gate noise. Reading out  $\Re[\rho_{01}]$  does not reveal any features from the latter, thus the effects from the former, which are not part of our model Eq. (3), are unveiled.

In Fig. 3(c), we compare the data for  $\Im[\rho_{01}]$  with the analytical prediction of Eq. (3). For small numbers of repetitive Mølmer-Sørensen gate pairs (e.g., 0, 3 and 5, corresponding to black up-pointing triangles, green left-pointing triangles and blue circles), increasing  $\theta_0$  reduces  $\Im[\rho_{01}]$ , as predicted by Eq. (3) (lines, where we have chosen the bit-flip rate  $p$  based on the fitting in Fig. 3(a)). However, for each fixed  $\theta_0$ , how  $\Im[\rho_{01}]$  changes with the number of repetitions cannot be fully resolved. This can be understood from Eq. (3): For small  $\theta_0$ , increasing  $p$  makes  $\Im[\rho_{01}]$  smaller, while for large  $\theta_0$ , increasing  $p$  makes  $\Im[\rho_{01}]$  larger. The  $\Im[\rho_{01}] - \theta_0$  curves for different  $p$  are therefore close to each other and cross each other. This is demonstrated in the blue solid, orange dot-dash-space, green dot-dot-space and red dashed lines in Fig. 3(c). In fact, this crossing is visible in the hardware data. For the third value of  $\theta_0$ ,  $\Im[\rho_{01}]$  for 0, 3 and 5 repetitions are the closest to each other compared with other  $\theta_0$ . In addition to the crossing lines, Eq. (3) also has the property that  $p = 0$  features the largest  $\theta_0$  dependence of  $\Im[\rho_{01}]$ . These suggest that unlike  $\rho_{00}$ ,  $\Im[\rho_{01}]$ , together with  $\Re[\rho_{01}]$ , is not ideal for resolving the dependence of the transformed logical channel on  $p$  and  $\theta_0$ . Finding suitable observables in addition to  $\rho_{00}$  remains an open question, which will be beneficial for evaluating how well the intrinsic noise of Mølmer-Sørensen gates is approximated as  $X_1 + X_2$ . For the large number of repetitive Mølmer-Sørensen gate pairs (15 repetitions here, red right-pointing triangles), the deviation from the model is more evident. However, we are able to observe one property that matches the model for large  $p$ :  $\Im[\rho_{01}]$  increases as  $\theta_0$  is increased from the third value to the fourth value.

In the Supplemental Material [28], we compare the data of  $\Im[\rho_{01}]$  with simulations of the compiled circuit under bit-flip noise. We did the simulation for  $\Re[\rho_{01}]$  as well, and the result is all zero. For comparison with trapped-ion entangling gates subject to the sum of bit-flip errors, we also run the modified bit-flip repetition code circuit Fig. 2(a) on the IQM Garnet quantum hardware, which is based on transmon qubits and whose entangling gates are unlikely to have bit-flip errors. As expected,

this results in a mismatch between the hardware data and our model Eq. (3). The details are in the Supplemental Material [28].

*Conclusion and discussion* — We present the first endeavour to demonstrate directly reshaping the native quantum device noise via modified quantum error correction codes, showing that this can be achieved in a predictable and deterministic way. Focusing on trapped-ion setups, we analytically find that the two-qubit entangling gate has dominant noise in the form of the sum of bit-flip errors. We then theoretically derive and experimentally verify how modified bit-flip repetition codes with extra tunability reshapes this noise into noise channels acting on the output logical qubit, which have structures different from the bit-flip error.

Our results open up many possibilities for future work along this direction. In the short term, optimal observables may be found to replace  $\rho_{01}$  for the verification of our model Eq. (3) on quantum devices. The inserted  $R_y$  gate for additional tunability may be replaced by other single-qubit gates to provide access to even more abundant structures of the resulting logical channels, and to possibly unveil other noise sources in trapped-ion entangling gates. In the long term, the combinations of quantum devices based on different physical mechanisms and error correction codes matching their dominant noise may be explored. One ambitious goal will be to directly use the reshaped logical error channel for simulations of open quantum dynamics.

*Acknowledgement* — We thank Hyukjoon Kwon for very helpful discussions. We acknowledge financial support from EPSRC EP/Y004752/1, EP/W032643/1, EP/Z53318X/1. This work was also supported by the National Research Foundation of Korea (NRF) grant funded by the Korea government (MSIT) (No. RS-2024-00413957).

- 
- [1] A. Montanaro, npj Quantum Information **2**, 1 (2016).  
 [2] J. Preskill, Quantum **2**, 79 (2018).  
 [3] A. K. Fedorov, N. Gisin, S. M. Beloussov, and A. I. Lvovsky, arXiv preprint arXiv:2203.17181 (2022).  
 [4] P. W. Shor, Physical review A **52**, R2493 (1995).  
 [5] A. R. Calderbank and P. W. Shor, Physical Review A **54**, 1098 (1996).  
 [6] A. Steane, Proceedings of the Royal Society of London. Series A: Mathematical, Physical and Engineering Sciences **452**, 2551 (1996).  
 [7] R. Raussendorf, Philosophical Transactions of the Royal Society A: Mathematical, Physical and Engineering Sciences **370**, 4541 (2012).  
 [8] E. T. Campbell, B. M. Terhal, and C. Vuillot, Nature **549**, 172 (2017).  
 [9] S. M. Girvin, arXiv preprint arXiv:2111.08894 (2021).  
 [10] I. Georgescu, Nature Reviews Physics **2**, 519 (2020).  
 [11] J. J. Wallman and J. Emerson, Physical Review A **94**, 052325 (2016).  
 [12] Y. Ma, M. Hanks, and M. Kim, Physical Review Letters **131**, 200602 (2023).  
 [13] A. G. Fowler, M. Mariantoni, J. M. Martinis, and A. N. Cleland, Physical Review A **86**, 032324 (2012).  
 [14] P. W. Shor, in *Proceedings of 37th conference on foundations of computer science* (IEEE, 1996) pp. 56–65.  
 [15] J. D. Guimarães, J. Lim, M. I. Vasilevskiy, S. F. Huelga, and M. B. Plenio, PRX Quantum **4**, 040329 (2023).  
 [16] Y. Ma and M. Kim, Physical Review A **109**, 012431 (2024).  
 [17] A. Sørensen and K. Mølmer, Physical Review A **62**, 022311 (2000).  
 [18] K. Mølmer and A. Sørensen, Physical Review Letters **82**, 1835 (1999).  
 [19] Y. Ma, M. C. Pace, and M. Kim, Physical Review A **106**, 012605 (2022).  
 [20] Y. Wang, S. Crain, C. Fang, B. Zhang, S. Huang, Q. Liang, P. H. Leung, K. R. Brown, and J. Kim, Physical Review Letters **125**, 150505 (2020).  
 [21] C. Fang, Y. Wang, S. Huang, K. R. Brown, and J. Kim, Physical Review Letters **129**, 240504 (2022).  
 [22] M. Kang, Y. Wang, C. Fang, B. Zhang, O. Khosravani, J. Kim, and K. R. Brown, Physical Review Applied **19**, 014014 (2023).  
 [23] C. J. Trout, M. Li, M. Gutiérrez, Y. Wu, S.-T. Wang, L. Duan, and K. R. Brown, New Journal of Physics **20**, 043038 (2018).  
 [24] D. M. Debroy, M. Li, S. Huang, and K. R. Brown, Quantum Science and Technology **5**, 034002 (2020).  
 [25] K. Sun, M. Kang, H. Nuomin, G. Schwartz, D. N. Beratan, K. R. Brown, and J. Kim, arXiv preprint arXiv:2405.14624 (2024).  
 [26] D. Maslov, New Journal of Physics **19**, 023035 (2017).  
 [27] Getting started with native gates, <https://ionq.com/docs/getting-started-with-native-gates>, accessed: 2024-05-21.  
 [28] See the supplemental information.  
 [29] C. Monroe, W. C. Campbell, L.-M. Duan, Z.-X. Gong, A. V. Gorshkov, P. W. Hess, R. Islam, K. Kim, N. M. Linke, G. Pagano, *et al.*, Reviews of Modern Physics **93**, 025001 (2021).  
 [30] M. Foss-Feig, G. Pagano, A. C. Potter, and N. Y. Yao, arXiv preprint arXiv:2409.02990 (2024).  
 [31] Y. Nam, J.-S. Chen, N. C. Panti, K. Wright, C. Delaney, D. Maslov, K. R. Brown, S. Allen, J. M. Amini, J. Apisdorf, *et al.*, npj Quantum Information **6**, 33 (2020).  
 [32] K. Wright, K. M. Beck, S. Debnath, J. Amini, Y. Nam, N. Grzesiak, J.-S. Chen, N. Panti, M. Chmielewski, C. Collins, *et al.*, Nature communications **10**, 5464 (2019).  
 [33] braket circuits gate module, [https://amazon-braket-sdk-python.readthedocs.io/en/latest/\\_apidoc/braket.circuits.html](https://amazon-braket-sdk-python.readthedocs.io/en/latest/_apidoc/braket.circuits.html), accessed: 2024-05-21.  
 [34] E. B. Wilson, Journal of the American Statistical Association **22**, 209 (1927).

# Supplemental Material: Reshaping quantum device noise via quantum error correction

Yue Ma<sup>1</sup>, Michael Hanks<sup>1</sup>, Evdokia Gneusheva<sup>1</sup>, and M. S. Kim<sup>1</sup>  
<sup>1</sup>*Blackett Laboratory, Imperial College London,  
 SW7 2AZ, United Kingdom*

In this Supplemental Material, we first analyze the nontrivial structure of the output logical channel, Eq. (3) in the main text. We then derive a class of generalised modified bit-flip codes, where a general single-qubit gate is inserted between the encoding and the decoding process. Next, we present the analytical and numerical details of deriving the noise of Mølmer-Sørensen gates under dephasing of the oscillation mode. We then explain the technical details of implementing the quantum circuits, Fig. 2 in the main text, on the IonQ Aria-1 quantum device. We next give a detailed description of conventions and gate decompositions that we have used. Afterwards we provide the full compiled circuits that we implement on the IonQ Aria-1 quantum device. Then we present our results of noisy simulations of the compiled quantum circuits. Finally we demonstrate the reshaping of noise with the three-qubit bit-flip repetition code on a superconducting qubit quantum device, the IQM Garnet, and characterize its native Controlled-Z (CZ) gate.

## I. NONTRIVIAL LOGICAL NOISE CHANNEL AFTER RESHAPING

Equation (3) in the main text demonstrates how the modified bit-flip repetition code reshapes the original noise channel acting on the physical qubits, namely, the bit-flip channel with Kraus operators  $\{F_I = \sqrt{1-p}I, F_X = \sqrt{p}X\}$ . If we choose  $\theta_0 = 0$ , that is, no  $R_y$  gate is acted on qubit 1, the channel expressed by Eq. (3) in the main text is consistent with the success probability  $p_{\text{success}}$  of the code. As the value of  $\theta_0$  is increased, logical  $Y$  and  $Z$  operators start to contribute to the channel. If we take  $\theta_0 = \pi$ , the channel is entirely made of the stochastic mixture of logical  $Y$  and  $Z$  operators. The weights of the logical operators are nontrivially correlated with each other, as shown in Eq. (3) in the main text. This is fundamentally different from the partial probabilistic error cancellation scheme in Ref. [1], where classical post-processing modifies the weight of each Pauli operator individually. The correlation in Eq. (3) in the main text implies that our method of reshaping the native noise via quantum error correction codes has the potential of defining novel nontrivial hierarchies for what target quantum channels are easier to be simulated, even when the original noise channels do not have particular structures (e.g. Pauli noise). In Sec. II, as a first step in this direction, we generalise the  $R_y$  gate to a general single-qubit gate parameterised by three angles, and show the resulting logical quantum channel.

## II. INSERTING A GENERAL SINGLE-QUBIT GATE TO THE BIT-FLIP REPETITION CODE

Here we generalise the result of Eq. (3) in the main text by replacing the gate Eq. (2) in the main text applied to the first qubit with a general single-qubit unitary operator. Any unitary operator applied to one qubit can

be parameterised by three angles: [2]

$$U(\theta, \phi, \delta) = \begin{pmatrix} \exp(i\phi) \cos(\theta) & -\exp(-i\delta) \sin(\theta) \\ \exp(i\delta) \sin(\theta) & \exp(-i\phi) \cos(\theta) \end{pmatrix}, \quad (1)$$

where  $0 \leq \theta \leq \pi/2$ ,  $0 \leq \phi \leq 2\pi$ ,  $0 \leq \delta \leq 2\pi$ . After syndrome measurements and corrections, the final state is derived to be

$$\begin{aligned} \bar{\rho}_f = & (1+p)(1-p)^2 \cos^2(\theta) R_1 |\bar{\psi}\rangle \langle \bar{\psi}| R_1^\dagger \\ & + (2-p)(1-p)p \sin^2(\theta) R_2 |\bar{\psi}\rangle \langle \bar{\psi}| R_2^\dagger \\ & + (2-p)p^2 \cos^2(\theta) R_3 |\bar{\psi}\rangle \langle \bar{\psi}| R_3^\dagger \\ & + p(1+p)(1-p) \sin^2(\theta) R_4 |\bar{\psi}\rangle \langle \bar{\psi}| R_4^\dagger \\ & + (1-p)^3 \sin^2(\theta) R_5 |\bar{\psi}\rangle \langle \bar{\psi}| R_5^\dagger \\ & + p^2(1-p) \cos^2(\theta) R_6 |\bar{\psi}\rangle \langle \bar{\psi}| R_6^\dagger \\ & + p^3 \sin^2(\theta) R_7 |\bar{\psi}\rangle \langle \bar{\psi}| R_7^\dagger \\ & + p(1-p)^2 \cos^2(\theta) R_8 |\bar{\psi}\rangle \langle \bar{\psi}| R_8^\dagger, \end{aligned} \quad (2)$$

with

$$\begin{aligned} R_1 &= \begin{pmatrix} \exp(i\phi) & 0 \\ 0 & \exp(-i\phi) \end{pmatrix}, R_2 = \begin{pmatrix} 0 & -\exp(-i\delta) \\ \exp(i\delta) & 0 \end{pmatrix}, \\ R_3 &= \begin{pmatrix} 0 & \exp(i\phi) \\ \exp(-i\phi) & 0 \end{pmatrix}, R_4 = \begin{pmatrix} -\exp(-i\delta) & 0 \\ 0 & \exp(i\delta) \end{pmatrix}, \\ R_5 &= \begin{pmatrix} \exp(i\delta) & 0 \\ 0 & -\exp(-i\delta) \end{pmatrix}, R_6 = \begin{pmatrix} 0 & \exp(-i\phi) \\ \exp(i\phi) & 0 \end{pmatrix}, \\ R_7 &= \begin{pmatrix} 0 & \exp(i\delta) \\ -\exp(-i\delta) & 0 \end{pmatrix}, R_8 = \begin{pmatrix} \exp(-i\phi) & 0 \\ 0 & \exp(i\phi) \end{pmatrix}. \end{aligned}$$

## III. DETAILS OF NOISY MØLMER-SØRENSEN GATES

The implementation of Mølmer-Sørensen gates [3, 4] in trapped-ion systems involve two ions whose intrinsic

energy levels are considered as qubits, and their common vibrational mode which is modelled as a mechanical oscillator whose virtual excitation by the laser field is used to entangle the intrinsic states of the two ions. The Hamiltonian is generally referred to as [4]

$$H = f(t)J_y x + g(t)J_y p, \quad (3)$$

where  $J_y = (\sigma_{y1} + \sigma_{y2})/2$ ,  $\sigma_{yi}$  are Pauli operators,  $f(t) = -\sqrt{2}\eta\Omega \cos(\nu - \delta)t$ ,  $g(t) = -\sqrt{2}\eta\Omega \sin(\nu - \delta)t$ , where  $\eta$  is the Lamb-Dicke parameter,  $\Omega$  is the Rabi frequency,  $\nu$  is the mechanical frequency,  $\delta$  is the laser detuning,  $x$  and  $p$  are the dimensionless position and momentum operators, respectively. We want to derive the quantum channel that connects the final state subject to noise with the target state. We therefore work in the interaction picture with respect to the unitary evolution governed by Eq. (3) [4]. In this way, the dynamics in the interaction picture directly correspond to our desired quantum channel.

The dominant source of noise for trapped ion systems is the motional dephasing [5]. In the Lindblad form, this corresponds to the dissipator  $C = \sqrt{\Gamma_P} a^\dagger a$ . After moving into the interaction picture, the dissipator becomes

$$\tilde{C} = \sqrt{\Gamma_P} (a^\dagger + J_y \frac{G(t) + iF(t)}{\sqrt{2}}) (a + J_y \frac{G(t) - iF(t)}{\sqrt{2}}), \quad (4)$$

where  $G(t) = \int_0^t dt' g(t')$ ,  $F(t) = \int_0^t dt' f(t')$ , and the dynamics become

$$\frac{d}{dt} \tilde{\rho}(t) = -\frac{1}{2} \tilde{C}^\dagger \tilde{C} \tilde{\rho} - \frac{1}{2} \tilde{\rho} \tilde{C}^\dagger \tilde{C} + \tilde{C} \tilde{\rho} \tilde{C}^\dagger. \quad (5)$$

We approximate that throughout the evolution, in this interaction picture, the state of the two qubits remains separable from the state of the oscillator, which stays in the initial thermal state. Specifically, we assume  $\tilde{\rho}(t) \approx \tilde{\rho}_q(t) \otimes \gamma_\nu$ , where  $\tilde{\rho}_q(t)$  is the joint state of the two qubits, and  $\gamma_\nu$  is the thermal state of the oscillator with mean phonon number  $n_{\text{th}}$ . Under this approximation and taking the partial trace over the oscillator mode, Eq. (5) becomes the dynamical equation for only the state

of the qubits,

$$\begin{aligned} \frac{d}{dt} \tilde{\rho}_q(t) = & \\ (G^2(t) + F^2(t))(n_{\text{th}} + \frac{1}{2})\Gamma_P & (-\frac{1}{2}J_y^2 \tilde{\rho}_q - \frac{1}{2}\tilde{\rho}_q J_y^2 + J_y \tilde{\rho}_q J_y) \\ + \frac{1}{4}(G^2(t) + F^2(t))^2 \Gamma_P & (-\frac{1}{2}J_y^4 \tilde{\rho}_q - \frac{1}{2}\tilde{\rho}_q J_y^4 + J_y^2 \tilde{\rho}_q J_y^2). \end{aligned} \quad (6)$$

The equation can be straightforwardly solved in an element-wise manner by expanding all operators in the eigenbasis of  $J_y$  [4]. We are interested in interaction times when the state of the qubits disentangles with the state of the oscillator in the original picture, and when the maximal entanglement between the two qubits is generated (up to local unitary operators that rotate  $Y$  into  $X$ , this will be referred to as XX gates later). These correspond to the constraints between parameters [4],  $\tau = 2\pi K/(\nu - \delta)$  and  $\eta\Omega/(\nu - \delta) = 1/2\sqrt{K}$ , where  $K$  is an integer referring to how many phase-space loops of the oscillator have been traversed [6]. For simplicity, we define two parameters

$$r_1 = \frac{1}{4}(2n_{\text{th}} + 1)\Gamma_P \frac{\tau}{K}, \quad (7)$$

$$r_2 = \frac{1}{8}\Gamma_P \frac{3\tau}{2K^2}. \quad (8)$$

The quantum channel that maps the initial state  $\tilde{\rho}_q(0)$  to the final state  $\tilde{\rho}_q(\tau)$ , is found to have the following canonical Kraus operators ( $\text{Tr}(K_i^\dagger K_j) = 0$  for  $i \neq j$ )

$$\begin{aligned} K_1 &= a_1 I + a_3 J_y^2, \\ K_2 &= \sqrt{\frac{1}{2}(1 - e^{-4r_1})} J_y, \\ K_3 &= a_2 I + a_4 J_y^2, \end{aligned} \quad (9)$$

where  $a_1, a_2, a_3$  and  $a_4$  are solutions of the coupled equations

$$\begin{aligned} a_1^2 + a_2^2 &= 1, \\ a_1 a_3 + a_2 a_4 &= e^{-r_1 - r_2} - 1, \\ 2a_1 a_3 + a_3^2 + 2a_2 a_4 + a_4^2 &= \frac{1}{2}(e^{-4r_1} - 1), \\ 2a_1 a_2 + a_3 a_4 + a_1 a_4 + a_2 a_3 &= 0. \end{aligned} \quad (10)$$

Note that, the canonical Kraus representation of a quantum channel is unique. The non-uniquenesses in the solution of Eq. (10) are that we can simultaneously swap  $a_1$  with  $a_2$  and  $a_3$  with  $a_4$ , and that there are global phases for each Kraus operator in Eq. (9). Considering that practical Mølmer-Sørensen gates operate in the weak coupling regime [7–10], i.e, small phase-space loops are traversed many times, one canonical Kraus operator has a dominant identity component. We fix this to be  $K_1$ . We find that  $a_1 \approx 1$  has closed form solution, after removing the global phases by requiring  $a_1 > 0$  and  $a_2 > 0$ ,

$$a_1 = \sqrt{\frac{e^{-r_2}(4e^{2r_1} - e^{2r_2} + e^{4r_1+2r_2} + e^{r_2}\sqrt{16e^{6r_1} + e^{2r_2}(-1 + e^{4r_1})^2})}{2\sqrt{16e^{6r_1} + e^{2r_2}(-1 + e^{4r_1})^2}}} \quad (11)$$

The solution for  $a_2$ ,  $a_3$  and  $a_4$  will be found once Eq. (11) is inserted into Eq. (10).

As a practical example, we consider the weak-coupling parameters given in Ref. [4],  $\eta = 0.1$ ,  $\Omega = 0.1$ ,  $K = 25$ . For  $\Gamma_P = 0.02$  and  $n_{\text{th}} = 0.05$ , we find  $r_1 = 0.3456$  and  $r_2 = 0.0094$ . These lead to the solution  $a_1 = 0.9837$ ,  $a_2 = 0.1797$ ,  $a_3 = -0.2282$ ,  $a_4 = -0.4136$ . In particular,  $K_2 = 0.612J_y$  is the leading noise source, while  $K_1$  is close to the identity operator. Importantly,  $K_2$  represents the sum of bit-flip errors for each of the two qubits. Note that in theoretical derivations [4], the target gate is in the YY form, while for experimental trapped ion systems such as IonQ, the target gate is in the XX form. This implies that  $K_2$  in the experimental XX gate setup will be proportional to  $\sigma_{x1} + \sigma_{x2}$ , which is indeed the sum of bit-flip errors. We will show that this sum will be discretized by the syndrome measurements of the bit-flip repetition code, therefore the noisy Mølmer-Sørensen gates are directly compatible with the error assumptions of the codes.

We also numerically simulated the exact dynamics following the Hamiltonian Eq. (3) and the dephasing dissipator  $C$ . Using the diagonalization of the Choi matrix, we find that the structure of the canonical Kraus operators in Eq. (9) remains the same, while each parameter is slightly different. The results are shown in Fig. 1 in the main text. The numerical results match reasonably well with the analytical ones. In particular,  $K_2$  represents the dominant error term.

For comparison, we also derive the quantum channel for the heating of the oscillator. The approximate analytical solution of the master equation is already derived in Ref. [4], however, there the fidelity was calculated rather than the quantum channel. We find that, the canonical Kraus form of the quantum channel is also represented by Eq. (9). The coefficients correspond to directly replacing  $r_1 \rightarrow r$ ,  $r_2 \rightarrow 0$ ,  $\Gamma_P \rightarrow \Gamma$ , and  $n_{\text{th}}$  becoming the mean bath phonon number for the relaxation operators [4]. Exact numerical simulation also leads to the same structure as Eq. (9). We can therefore deduce that based on the state of the two qubits alone, we cannot distinguish whether the oscillator mode is subject to dephasing noise or heating noise.

#### IV. DETAILS OF IMPLEMENTING NOISE RESHAPING ON IONQ ARIA-1

The noisiest quantum operations on the IonQ Aria-1 quantum device are the two-qubit gates [11]. Two-qubit gates are essential for generating entanglement, in particular, for encoding into the code space and syndrome measurements in our modified repetition code. IonQ uses

the Mølmer-Sørensen gate [3] as the native two-qubit gate [12]. Specifically, it exploits the  $X$ - $X$  type interaction,  $\exp[-i(\pi/4)X_1X_2]$  for entangling qubits 1 and 2, which is commonly referred to as the XX gate [13]. This gate is equivalent to the more conventionally used CNOT gate upto local rotations (see Sec. V, where all the conventions are also defined).

The quantum circuit for implementing our modified three-qubit bit-flip repetition code is the one in Fig. 2(a) in the main text. We have chosen to use four values of  $\theta_0$  in the  $R_y$  rotation,  $\theta_0/\pi \in \{0.01, 0.328, 0.647, 0.965\}$ . The  $R_x$  gate corresponds to the initialisation to  $\alpha|0\rangle + \beta|1\rangle$ , where  $\alpha = \cos(\phi/2)$  and  $\beta = -i\sin(\phi/2)$ . We have chosen  $\phi = \pi/9$ . The two CNOT gates between the  $R_x$  gate and the  $R_y$  gate correspond to the encoding process to the state  $|\psi\rangle$ . The four CNOT gates after the  $R_y$  gate are for the syndrome measurement and correction process. Qubits 4 and 5 are the ancillae and are measured in the computational basis. The outcomes (0, 0), (0, 1), (1, 0) and (1, 1) correspond to the four lines in Table 1 in the main text, respectively. Correction gates should be applied accordingly to bring the logical state back to the code space, which is spanned by  $\{|000\rangle, |111\rangle\}$ . However, as Amazon Braket does not support mid-circuit measurements, here we directly measure the three physical qubits (labelled 1,2,3) in the computational basis. Post-processing of the classical measurement results after many shots lead to the statistical estimation of the diagonal element of the final logical state  $\bar{\rho}_f$ , i.e.,  $\langle 000|\bar{\rho}_f|000\rangle \equiv \rho_{00}$ . Note that, this scheme including two ancillae can account for some measurement errors, as we only count measurement results that are compatible with the code space basis as valid.

The circuit in Fig. 2(a) in the main text needs to be rewritten into the combination of IonQ native gates, which include GPI1 and GPI2 for single-qubit gates and Mølmer-Sørensen gates for two-qubit entangling gates [12]. We manually compile the circuit in order to keep a clear structure. To be specific, we first decompose the CNOT gate in terms of the  $XX$  gate and  $R_x$ ,  $R_y$ ,  $R_z$  gates (see Sec. V). We then convert these gates into the native gates, keeping track of the phase of each qubit so that a virtual  $R_z$  gate is applied to each qubit at the end of the circuit [12]. The virtual  $R_z$  gates are not actually implemented at the hardware level as the qubits are only measured in the basis  $\{|0\rangle, |1\rangle\}$ . However, as they are propagated till the end of the circuit, it is no longer possible to separate the circuit into encoding section and decoding section. Instead, what is clear is that the first two Mølmer-Sørensen gates, which are between qubits labelled as (1, 2) and as (1, 3), encode the quantum information into the logical state, as they are associated with the first two CNOT gates in Fig. 2(a) in the main



text. Moreover, they are applied before the gates related to the tunable parameter  $\theta_0$  are applied. This gives us a direct connection with the circuit-agnostic analytical model, Eq. (3) in the main text, where the stochastic bit-flip errors are applied before the unitary rotation. Indeed, given that the implementation of Mølmer-Sørensen gates is much noisier than the GPi1 and GPi2 gates, we add in the tunability of the level of noise in the circuit by repeatedly inserting [14, 15] different numbers of redundant pairs of Mølmer-Sørensen gates that correspond to the identity operator in the noiseless case, after each of the two encoding Mølmer-Sørensen gates (see Sec. VI for the actual circuits we have run on the quantum device).

The diagonal element  $\rho_{00}$  itself does not provide a full picture of the logical channel which is reshaped from the native device noise via our modified bit-flip repetition codes. We are going to show that we have also measured the off-diagonal element,  $\langle 000 | \bar{\rho}_f | 111 \rangle \equiv \rho_{01}$ , from the quantum device. However, if we were to directly get  $\rho_{01}$  from the quantum circuit Fig. 2(a) in the main text, quantum gates that involve the weighted sum of the logical operators  $X_L$  and  $Z_L$  need to be applied, which act on the three physical qubits simultaneously and are thus difficult and noisy to implement on the IonQ device. We therefore make use of different quantum circuits here to experimentally extract the complex value of  $\rho_{01}$ , using only three qubits without ancillae. The circuits are shown in Fig. 2(b) in the main text. It is straightforward to check that this circuit (without the final gate  $U_\rho$  for extracting the logical density matrix elements via computational basis measurements) is equivalent to the one in Fig. 2(a) in the main text, using ZX calculus [16]. The value of  $\rho_{01}$  (and  $\rho_{00}$  for comparison with Fig. 2(a) in the main text) is constructed in the following way.

*Case 1.*  $U_\rho$  is chosen as the identity operator. We construct:

$$\frac{\text{the number of trials in the table below}}{\text{the total number of trials}} \Rightarrow \rho_{00} \quad (12)$$

with the table as

qubit 1	qubit 2	qubit 3
0	0	0
0	0	1
0	1	0
1	1	1

*Case 2.*  $U_\rho$  is chosen as  $R_y(\pi/2)R_z(-\pi)$ . We construct:

$$\frac{\text{the number of trials in the table below}}{\text{the total number of trials}} - \frac{1}{2} \Rightarrow \Re[\rho_{01}] \quad (13)$$

with the table as

*Case 3.*  $U_\rho$  is chosen as  $R_y(\pi/2)R_z(-\pi/2)$ . We construct:

$$\frac{\text{the number of trials in the table below}}{\text{the total number of trials}} - \frac{1}{2} \Rightarrow \Im[\rho_{01}] \quad (14)$$

with the table as

qubit 1	qubit 2	qubit 3
0	0	0
0	0	1
0	1	0
0	1	1

qubit 1	qubit 2	qubit 3
0	0	0
0	0	1
0	1	0
1	1	1

## V. CONVENTIONS AND GATE DECOMPOSITIONS

In this section, we first clarify the conventions we have followed for using the IonQ Aria-1 quantum device via Amazon Braket. We then illustrate the gate decompositions, namely, how CNOT gate, XX gate and Mølmer-Sørensen gates with different phases are related.

For expressing quantum operators as matrices, we follow the conventions of Amazon Braket [17]. Specifically, the qubit computational basis is given by

$$|0\rangle = \begin{pmatrix} 1 \\ 0 \end{pmatrix}, \quad |1\rangle = \begin{pmatrix} 0 \\ 1 \end{pmatrix}. \quad (15)$$

The CNOT gate, where qubit 1 is the control and qubit 2 is the target, is

$$\begin{aligned} \text{CNOT} &= |0\rangle_1 \langle 0| \otimes I_2 + |1\rangle_1 \langle 1| \otimes X_2 \\ &= \begin{pmatrix} 1 & 0 & 0 & 0 \\ 0 & 1 & 0 & 0 \\ 0 & 0 & 0 & 1 \\ 0 & 0 & 1 & 0 \end{pmatrix}. \end{aligned} \quad (16)$$

The single-qubit rotations are

$$R_x(\phi) = \begin{pmatrix} \cos(\phi/2) & -i \sin(\phi/2) \\ -i \sin(\phi/2) & \cos(\phi/2) \end{pmatrix}, \quad (17)$$

and

$$R_z(\phi) = \begin{pmatrix} \exp(-i\phi/2) & 0 \\ 0 & \exp(i\phi/2) \end{pmatrix}, \quad (18)$$

while  $R_y$  is already introduced in Eq. (2) in the main text. Mølmer-Sørensen gates, which are the native two-qubit entangling gates implemented on IonQ Aria-1, include

two phase parameters  $\phi_1$  and  $\phi_2$ ,

$$\text{MS}(\phi_1, \phi_2) = \frac{1}{\sqrt{2}} \times \begin{pmatrix} 1 & 0 & 0 & -ie^{-i(\phi_1+\phi_2)} \\ 0 & 1 & -ie^{-i(\phi_1-\phi_2)} & 0 \\ 0 & -ie^{i(\phi_1-\phi_2)} & 1 & 0 \\ -ie^{i(\phi_1+\phi_2)} & 0 & 0 & 1 \end{pmatrix}. \quad (19)$$

Their relation to the CNOT gate via the XX gate is illustrated in Fig. 1.

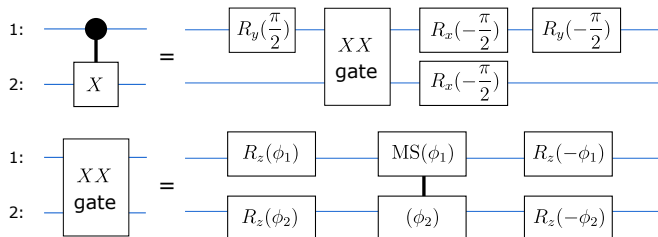


FIG. 1. The relation between the CNOT gate, the XX gate and the Mølmer-Sørensen gates. **(Top)** The CNOT gate can be decomposed as a combination of single-qubit rotations and the XX gate. **(Bottom)** The XX gate can be decomposed as the Mølmer-Sørensen gate  $\text{MS}(\phi_1, \phi_2)$  sandwiched by single-qubit  $R_z$  rotations.

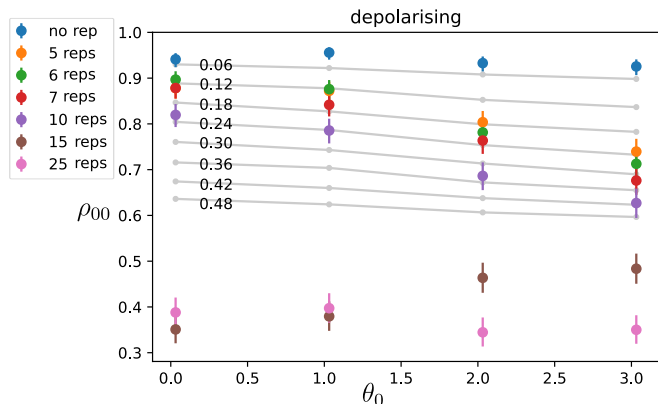


FIG. 2. Comparing the data from the IonQ Aria-1 device with the results from the noisy simulations of quantum circuits, for the value of  $\rho_{00}$ , i.e., the diagonal element of the output logical state. The points with error bars correspond to the data, where certain numbers of redundant pairs of Mølmer-Sørensen gates have been added in the quantum circuit with native gates in order to tune the error rate. Each data point corresponds to an average over 1000 shots. Error bars are 95% confidence intervals computed from the Wilson score [18]. The gray lines correspond to the simulation results with added depolarising noise channel, as described in the text. The depolarising rate  $p_{\text{dpl}}$  is marked on every line.

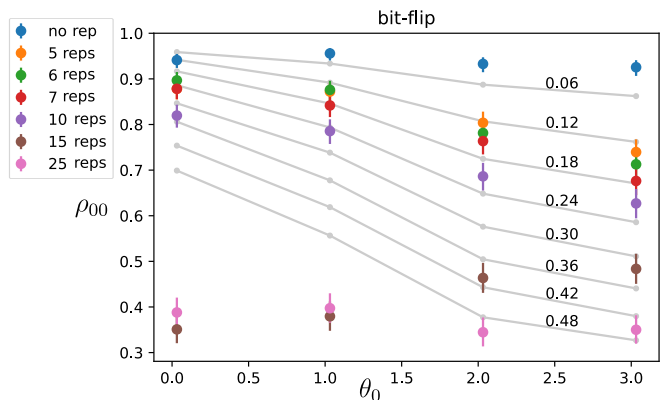


FIG. 3. Comparing the data from the IonQ Aria-1 device with the results from the noisy simulations of quantum circuits, for the value of  $\rho_{00}$ , i.e., the diagonal element of the output logical state. The points with error bars correspond to the data, where certain numbers of redundant pairs of Mølmer-Sørensen gates have been added in the quantum circuit with native gates in order to tune the error rate. Each data point corresponds to an average over 1000 shots. Error bars are 95% confidence intervals computed from the Wilson score [18]. The gray lines correspond to the simulation results with added bit-flip noise channel, as described in the text. The bit-flip rate  $p_{\text{bf}}$  is marked on every line.

## VI. THE COMPILED CIRCUITS IMPLEMENTED ON THE IONQ ARIA-1 QUANTUM DEVICE

The compiled circuits for the modified repetition code circuit shown in Fig. 2(a) in the main text that were run on the IonQ Aria-1 device are shown in Fig. 5, corresponding to the data points in Fig. 3(a) in the main text except the black triangles pointing to the left. The four values of  $\theta_0$  change the parameters of the GPI2 gates and Mølmer-Sørensen gates that are highlighted in red, where the first, second, third and fourth line inside the red blocks corresponds to the first, second, third and fourth value of  $\theta_0$ , respectively. The redundant pairs of Mølmer-Sørensen gates are marked in blue. Our definition of each repetition, as used in Fig. 3 in the main text, is that both pairs as circled in blue dotted lines are repeated. For example, for 5 repetitions, we will add 10 pairs of redundant Mølmer-Sørensen gates altogether. Note that the parameters of these redundant Mølmer-Sørensen gates are independent of the values of  $\theta_0$ .

## VII. NOISY SIMULATIONS OF QUANTUM CIRCUITS

In the main text, we have matched the data from the IonQ Aria-1 quantum device with the analytical model that does not explicitly consider any quantum circuits (see Fig. 3 and Eq. (3) in the main text). Here in this section, we are going to show how to match the data with

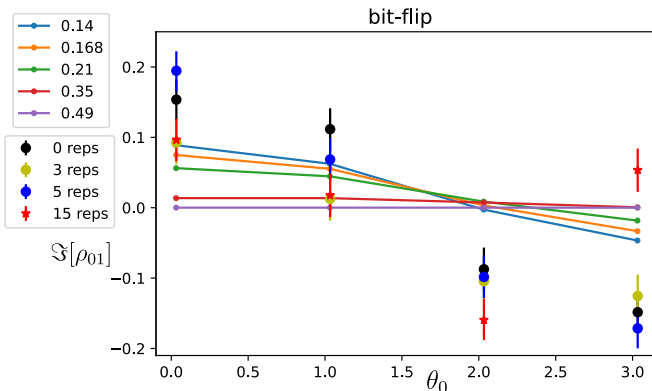


FIG. 4. Comparing the data from the IonQ Aria-1 device with the results from the noisy simulations of quantum circuits, for the value of  $\Im[\rho_{01}]$ , i.e., the imaginary part of the off-diagonal element of the output logical state. The quantum circuits are based on Fig. 2(b) in the main text and compiled to the native gates, having a very similar structure as Fig. 5. In particular, the encoding part of the circuit (until the fourth group in Fig. 5, also see the descriptions in the text), including the redundant Mølmer-Sørensen gate pairs, are the same as Fig. 5. The points with error bars correspond to the data, where certain numbers of redundant pairs of Mølmer-Sørensen gates have been added in the quantum circuit with native gates in order to tune the error rate. Each data point corresponds to an average over 1000 shots. Error bars are 95% confidence intervals computed from the Wilson score [18]. The lines correspond to the simulation results with added bit-flip noise channel, as described in the text. The bit-flip rates  $p_{bf}$  are listed in the legend.

noisy simulations of quantum circuits.

We consider the quantum circuits made of native gates of the IonQ Aria-1 quantum device. For simulating  $\rho_{00}$ , the circuits are shown in Fig. 5, except that we do not add in the redundant pairs of Mølmer-Sørensen gates as circled in blue dotted line, as on the simulator every quantum element is modelled as perfect. In order to mimic the effect of noise on the actual quantum device, we need to add in noise in the simulator. We replace the the redundant pairs of Mølmer-Sørensen gates with noise channels. We have chosen to use the predefined noise channels in Amazon Braket. Specifically, we have considered two models. The first one is the depolarising noise channel. After each of the two Mølmer-Sørensen gates that are followed by the blue circled blocks in Fig. 5, we add a depolarising noise channel for each of the qubit involved with depolarising rate  $p_{dpl}$ . That is, we have added altogether four depolarising noise channels. The second model is the bit-flip noise channel. The positions of these channels are the same as those in the first model. These channels are the bit-flip channel with bit-flip rate  $p_{bf}$ .

Fig. 2 shows the results of noisy simulations with added depolarising noise, while Fig. 3 is for the results of noisy simulations with added bit-flip noise. The slopes of the gray lines indicate that, for small  $\theta_0$ , depolarising noise

fits better with the data, while for large  $\theta_0$ , bit-flip noise fits better. This is compatible with the fact that the quantum error correction code we work on before inserting the  $R_y$  gate is designed to correct the bit-flip error. As seen in Fig. 3, along each gray line, the values of  $\rho_{00}$  increases drastically as  $\theta_0$  changes from the second value to the first value. The large population of  $\rho_{00}$  at  $\theta_0 \approx 0$  predicted by the noisy simulations is a result of bit-flip errors getting corrected by the repetition code. For the actual data obtained from the quantum device, however, there exists other sources of noise in addition to bit-flip noise. After the bit-flip errors are largely corrected by the code itself, the contributions from the remaining sources of error do not have a particular structure. Thus the change of  $\rho_{00}$  from the first value to the second value of  $\theta_0$  is better described by the depolarising noise channel, as seen in Fig. 2.

We have also tried to match the data of  $\Re[\rho_{01}]$  and  $\Im[\rho_{01}]$  with the noisy simulations of quantum circuits. The quantum circuits before compilation for obtaining them by only measurements in the computational basis are shown in Fig. 2(b) in the main text. The compiled circuits are similar to the ones shown in Fig. 5 for measuring  $\rho_{00}$ , as described in details in the caption of Fig. 4. We add bit-flip noise in the simulation, replacing the redundant pairs of Mølmer-Sørensen gates, same as the procedure described above. For  $\Re[\rho_{01}]$ , the noisy circuit simulation always has the result  $\Re[\rho_{01}] = 0$ , the same as that predicted in Fig. 3(b) in the main text based on the analytical circuit-agnostic model. For  $\Im[\rho_{01}]$ , the results are shown in Fig. 4. Similar to Fig. 3(c) in the main text based on the analytical circuit-agnostic model, the data do not quantitatively match the noisy circuit simulation. This is partly because the relevant numbers are small, therefore it is difficult to distinguish from the noise level and reach a small error bar. Another possible reason is that the dependence of  $\Im[\rho_{01}]$  on  $\theta_0$  and  $p_{bf}$  is not strong enough to be resolved on the quantum device that has complicated noise sources. In particular, this dependence is not sensitive to the dominant noise source, which is from the repeated Mølmer-Sørensen gates whose errors are bit-flip like.

## VIII. RESHAPING OF NOISE WITH IQM GARNET

We first transpile the modified three-qubit bit-flip repetition code circuit (Fig. 2(a) in the main text) into the native gate set of the IQM Garnet quantum device. Then we compare the hardware results from IQM Garnet with local simulations of the effects of increasing bit-flip, phase-flip, and depolarising errors on the transpiled circuit.

### A. Native Gate Set of IQM Garnet

The native gate set of the IQM Garnet quantum device [19] includes the single-qubit PhaseRx (PRx) gates and two-qubit Controlled-Z gates. Here is the matrix representation of these gates:

$$\text{PRx}(\theta, \phi) = \begin{pmatrix} \cos(\theta/2) & -ie^{-i\phi} \sin(\theta/2) \\ -ie^{i\phi} \sin(\theta/2) & \cos(\theta/2) \end{pmatrix} \quad (20)$$

and

$$\text{CZ} = \begin{pmatrix} 1 & 0 & 0 & 0 \\ 0 & 1 & 0 & 0 \\ 0 & 0 & 1 & 0 \\ 0 & 0 & 0 & -1 \end{pmatrix}, \quad (21)$$

where, in the computational basis, CZ gate flips the phase of the target qubit if the control qubit is in the  $|1\rangle$  state.

### B. Mapping of CNOT to CZ Gates

We begin by running the three-qubit bit-flip repetition code with the added  $R_y$  gate (main text Fig. 2(a)) on the IQM Garnet quantum device. This allows us to obtain the transpiled version of the circuit directly from the returned results of the quantum device, see Fig. 6.

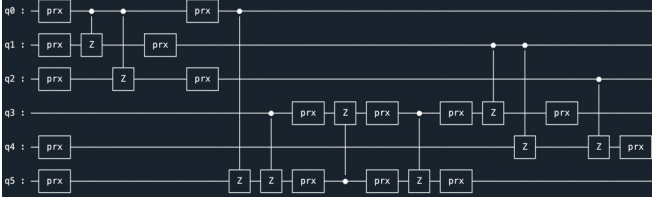


FIG. 6. Quantum circuit for the three-qubit bit-flip repetition code with an added tunable single-qubit rotation gate  $R_y(\theta_0)$  expressed with PRx and CZ gates.

Note that this circuit representation remains the same for different values of  $\theta_0$ . Also, note that the hardware, which has 20 qubits in total, used qubits 3, 4, 8, 9, 13, and 14 to run the circuit, which we mapped and re-labeled as qubits 0, 1, 2, 3, 4, and 5. Qubit 0 was mapped to qubit 9, qubit 1 to qubit 8, qubit 2 to qubit 4, qubit 3 to qubit 13, qubit 4 to qubit 3, and qubit 5 to qubit 14. Qubit 5 is an extra qubit added for transpilation purposes by the compiler, and it is very likely that SWAP operations were implemented due to qubit connectivity. Figure 7 is the qubit connectivity map for the IQM Garnet hardware, where we have identified in red the qubits used to implement our circuit:

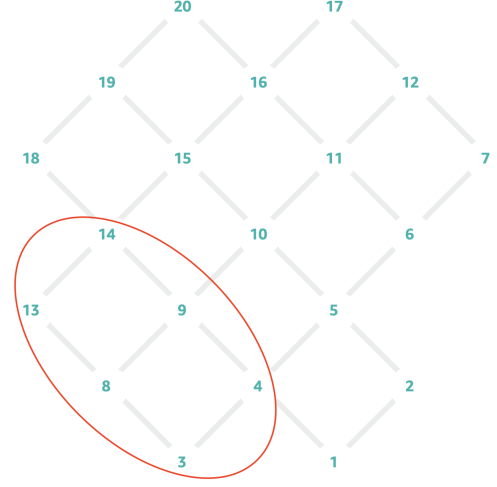


FIG. 7. Qubit connectivity map for the IQM Garnet quantum device.

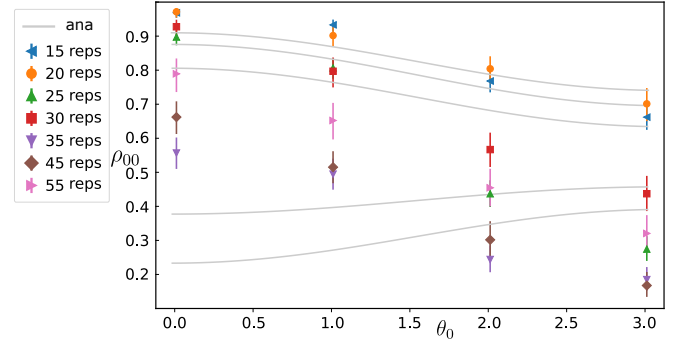


FIG. 8. Measurement results obtained from the IQM Garnet quantum device averaged over 1000 shots, in comparison with the analytical circuit-agnostic model of Eq. (3) in the main text, where the grey lines correspond to different bit-flip error rates  $p$ . See the text for more details.

We can establish the following equivalence between the

CNOT and CZ with PRx gates, up to a global phase:

$$\begin{aligned}
\text{CNOT} &= H \text{ CZ } H \\
&= \frac{1}{\sqrt{2}} \begin{pmatrix} 1 & 1 \\ 1 & -1 \end{pmatrix} \begin{pmatrix} 1 & 0 & 0 & 0 \\ 0 & 1 & 0 & 0 \\ 0 & 0 & 1 & 0 \\ 0 & 0 & 0 & -1 \end{pmatrix} \frac{1}{\sqrt{2}} \begin{pmatrix} 1 & 1 \\ 1 & -1 \end{pmatrix} \\
&= \begin{pmatrix} \cos(\pi/4) & -\sin(\pi/4) \\ \sin(\pi/4) & \cos(\pi/4) \end{pmatrix} \begin{pmatrix} \cos(\pi/2) & -i\sin(\pi/2) \\ -i\sin(\pi/2) & \cos(\pi/2) \end{pmatrix} \\
&\quad \begin{pmatrix} 1 & 0 & 0 & 0 \\ 0 & 1 & 0 & 0 \\ 0 & 0 & 1 & 0 \\ 0 & 0 & 0 & -1 \end{pmatrix} \\
&\quad \begin{pmatrix} \cos(\pi/4) & -\sin(\pi/4) \\ \sin(\pi/4) & \cos(\pi/4) \end{pmatrix} \begin{pmatrix} \cos(\pi/2) & -i\sin(\pi/2) \\ -i\sin(\pi/2) & \cos(\pi/2) \end{pmatrix} \\
&= R_y\left(\frac{\pi}{2}\right) R_x(\pi) \text{ CZ } R_y\left(\frac{\pi}{2}\right) R_x(\pi) \\
&= \text{PRx}\left(\frac{\pi}{2}, \frac{\pi}{2}\right) \text{PRx}(\pi, 0) \text{ CZ } \text{PRx}\left(\frac{\pi}{2}, \frac{\pi}{2}\right) \text{PRx}(\pi, 0),
\end{aligned}$$

where the Hadamard gate is  $H = \frac{1}{\sqrt{2}} \begin{pmatrix} 1 & 1 \\ 1 & -1 \end{pmatrix}$ . It is

difficult to precisely map the original circuit (main text Fig. 2(a)) to the compiled one in Fig. 6, but it is evident that the first two CZ gates, which are between qubits labeled as (0, 1) and (0, 2) and correspond to the qubits (9, 8) and (9, 4) on the physical hardware, encode the quantum information into the logical state, as they are associated with the first two CNOT gates in main text Fig. 2(a). These gates are applied before the gates related to the tunable parameter  $\theta_0$ . Later, we demonstrate the tunability of the noise by inserting different numbers of redundant pairs of CZ gates after each of the two encoding CZ gates. These pairs correspond to the identity operator in the noiseless case.

### C. Implementation of the Transpiled Quantum Circuit with extra CZ Gates on IQM Garnet

We have established that the two encoding CZ gates, corresponding to the first two CNOT gates of the repetition code with the inserted  $R_y(\theta_0)$  gate, are located between qubits 9 and 8, and qubits 9 and 4 on the IQM Garnet hardware. The next step is to insert an increasing number of CZ gates after each of the two encoding CZ gates to amplify the noise that is naturally associated with the CZ gates.

We initialize the circuit as follows: we choose the angle for  $R_x$  from the circuit in main text Fig. 2(a) to be  $\phi = \pi/9$ . We will vary the angle of our tunable  $R_y(\theta_0)$  gate, using the same values of  $\theta_0$  as in the main text, specifically  $\theta_0 = 0.01\pi, 0.328\pi, 0.647\pi, 0.965\pi$ . We will run the compiled version of the circuit demonstrated in

Fig. 6 on the IQM Garnet device, and we are going to insert 15, 20, 25, 30, 35, 45, and 55 redundant pairs of CZ gates after each of the two encoding CZ gates.

The primary source of noise in the implementation of the CZ gate is  $1/f$  flux noise, originating from fluctuations in the magnetic flux through superconducting loops caused by material defects or environmental disturbances. This noise has been previously discussed as heavily affecting qubit phase. Additionally, parasitic ZZ interactions are also associated with the noise generated from imperfect CZ gate implementations [19].

Fig. 8 shows the measurement results obtained from running the three-qubit bit-flip repetition code with tunable single-gate operations, expressed using CZ and PRx gates, on the IQM Garnet quantum device. Each data point represents an average over 1000 shots, with error bars indicating 95% confidence intervals computed using the Wilson score. We varied the values of angle  $\theta_0$  and the number of inserted redundant CZ gate pairs. Adding a small number of redundant CZ gate pairs reveals the dependence of  $\rho_{00}$  on  $\theta_0$ . This includes 15, 20, 25, and 35 repetitions, corresponding to blue triangles, orange circles, green triangles, red squares, and purple triangles, respectively, on the plot. As  $\theta_0$  increases from 0 to  $\pi$ ,  $\rho_{00}$  consistently decreases. This indicates that we have successfully managed to tune the channel in a predictable way and that this tunability depends on both the profile and level of noise. The results obtained from the hardware demonstrate that the native noise of the device enables a useful feature. We observe that while the decrease in  $\rho_{00}$  with increasing  $\theta_0$  holds true for a larger number of redundant CZ gate pairs, the overall value of  $\rho_{00}$  starts to shift upward past 35 repetitions: the overall value of  $\rho_{00}$  for each  $\theta_0$  is higher for 45 repetitions (represented by brown diamonds) than for 35, and it is also higher for 55 repetitions (represented by pink triangle) than for 45. We superimposed the plot of the analytical, circuit-agnostic model, main text Eq. (3) in Fig.8. We observe that the analytical model does not match the results from the hardware. As the CZ gate is unlikely to have bit-flip noise, we do expect that there is no match.

### D. Simulations of the Effects of the Increasing Bit-Flip, Phase-Flip and depolarising Errors on the Transpiled Circuit

To further investigate the noise profile of CZ gates, we simulated the effects of increasing noise on the three-qubit bit-flip repetition code with a tunable  $R_y(\theta_0)$  gate constructed using CZ and PRx gates. In the simulator, adding redundant pairs of CZ gates does not alter the output logical state, as every quantum operation is modeled as perfect. Therefore, instead of inserting specific repetitions of the CZ gate, we added predefined noise channels in Amazon Braket to mimic the effect of noise on the actual quantum device. We simulated the effect of increasing bit-flip noise, phase-flip

noise, and depolarising noise by directly inserting these noise models into the circuit. To do this, we added the noise channels one at a time after each of the two encoding CZ gates: a CZ gate between qubits (9, 8) and a CZ gate between qubits (9, 4). We inserted two noise channels after each encoding CZ gate, resulting in four noise channels in total. The error rates were set to  $p = 0.06, 0.12, 0.18, 0.24, 0.30, 0.36, 0.42, 0.48$ , corresponding to the gray lines in Figures 9, 10, and 11. The simulations show the measurement results averaged over 10,000 shots. We compared these simulations with the hardware measurements to determine which noise model is most closely associated with the imperfect implementation of the CZ gate.

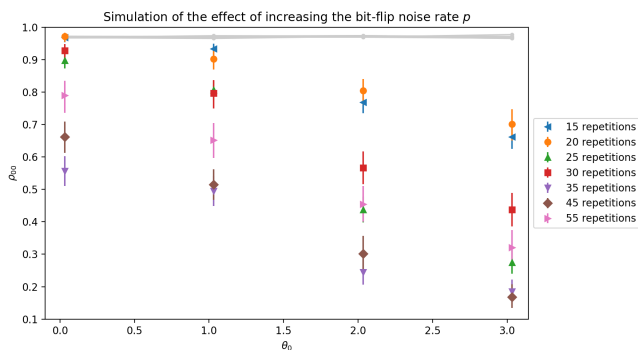


FIG. 9. Comparison of the data obtained from the IQM Garnet quantum device with the simulations results of quantum circuits including bit-flip noise.

The results of the noisy simulations with added bit-flip noise are shown in Fig. 9, while Fig. 10 displays the results for phase-flip noise, and Fig. 11 illustrates depolarising noise. As seen in Fig. 9, the bit-flip noise model does not fit the hardware results. We can deduce that the noise model associated with the CZ gate does not match bit-flip error noise model.

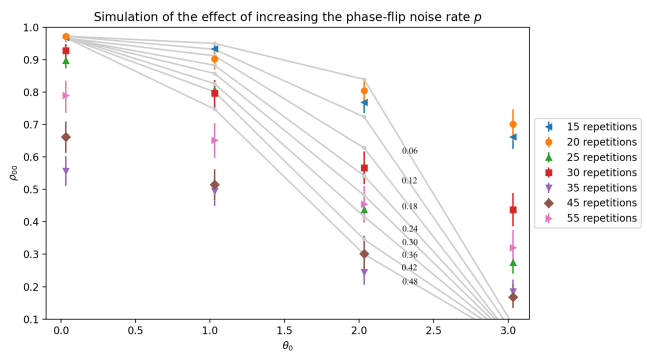


FIG. 10. Comparison of the data obtained from the IQM Garnet quantum device with the simulations results of quantum circuits including phase-flip noise.

Turning to the plot of noisy simulations with phase-flip errors (Fig. 10), we observe a better fit with the hardware data compared to the bit-flip error case. However, the slopes of the gray lines, which correspond to different phase-flip error rates, are steeper than the slopes of the data points from the IQM Garnet quantum device measurements. This indicates that the simulated phase-flip noise model does not fully match the hardware data, suggesting that the imperfect implementation of CZ gates generates a noise model which is not only phase-flip noise model but also a mix of other types of noise. Nonetheless, we confirm that phase-flip noise model, unlike bit-flip noise model, is a significantly better match with the noise of the CZ gate.

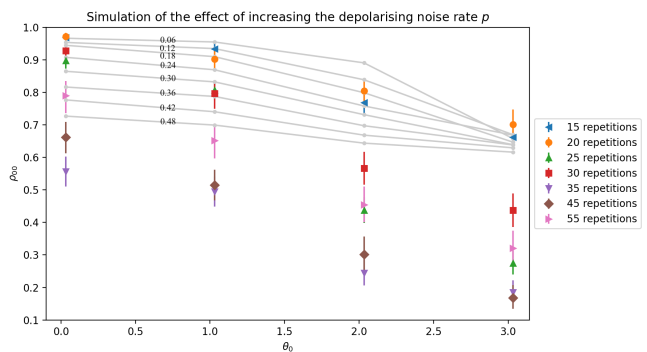


FIG. 11. Comparison of the data obtained from the IQM Garnet quantum device with the simulations results of quantum circuits including depolarising noise.

We interpret the simulations of increasing depolarising noise shown in Fig. 11 similarly. The plot of the depolarising noise model shows similarities with the hardware measurement results, suggesting that the noise generated by the imperfect realization of the CZ gate also includes depolarising noise model among other types. However, the slopes of the gray lines are shallower than the slopes of the hardware measurement data, indicating that depolarising noise alone does not fully account for the observed data and is not the only type of noise model present in the channel.

- 
- [1] J. D. Guimarães, J. Lim, M. I. Vasilevskiy, S. F. Huelga, and M. B. Plenio, *PRX Quantum* **4**, 040329 (2023).
- [2] K. Nemoto, *Journal of Physics A: Mathematical and General* **33**, 3493 (2000).
- [3] K. Mølmer and A. Sørensen, *Physical Review Letters* **82**, 1835 (1999).
- [4] A. Sørensen and K. Mølmer, *Physical Review A* **62**, 022311 (2000).
- [5] K. Sun, M. Kang, H. Nuomin, G. Schwartz, D. N. Beratan, K. R. Brown, and J. Kim, arXiv preprint arXiv:2405.14624 (2024).
- [6] Y. Ma, M. C. Pace, and M. Kim, *Physical Review A* **106**, 012605 (2022).
- [7] C. Monroe, W. C. Campbell, L.-M. Duan, Z.-X. Gong, A. V. Gorshkov, P. W. Hess, R. Islam, K. Kim, N. M. Linke, G. Pagano, *et al.*, *Reviews of Modern Physics* **93**, 025001 (2021).
- [8] M. Foss-Feig, G. Pagano, A. C. Potter, and N. Y. Yao, arXiv preprint arXiv:2409.02990 (2024).
- [9] Y. Nam, J.-S. Chen, N. C. Pimenti, K. Wright, C. Delaney, D. Maslov, K. R. Brown, S. Allen, J. M. Amini, J. Apisdorf, *et al.*, *npj Quantum Information* **6**, 33 (2020).
- [10] K. Wright, K. M. Beck, S. Debnath, J. Amini, Y. Nam, N. Grzesiak, J.-S. Chen, N. Pimenti, M. Chmielewski, C. Collins, *et al.*, *Nature communications* **10**, 5464 (2019).
- [11] Ionq aria, <https://ionq.com/quantum-systems/aria>, accessed: 2024-05-21.
- [12] Getting started with native gates, <https://ionq.com/docs/getting-started-with-native-gates>, accessed: 2024-05-21.
- [13] C. J. Trout, M. Li, M. Gutiérrez, Y. Wu, S.-T. Wang, L. Duan, and K. R. Brown, *New Journal of Physics* **20**, 043038 (2018).
- [14] Y. Wang, S. Crain, C. Fang, B. Zhang, S. Huang, Q. Liang, P. H. Leung, K. R. Brown, and J. Kim, *Physical Review Letters* **125**, 150505 (2020).
- [15] C. Fang, Y. Wang, S. Huang, K. R. Brown, and J. Kim, *Physical Review Letters* **129**, 240504 (2022).
- [16] M. Hanks, M. P. Estarellas, W. J. Munro, and K. Nemoto, *Physical Review X* **10**, 041030 (2020).
- [17] braket circuits gate module, [https://amazon-braket-sdk-python.readthedocs.io/en/latest/\\_apidoc/braket.circuits.html](https://amazon-braket-sdk-python.readthedocs.io/en/latest/_apidoc/braket.circuits.html), accessed: 2024-05-21.
- [18] E. B. Wilson, *Journal of the American Statistical Association* **22**, 209 (1927).
- [19] L. Abdurakhimov, J. Adam, H. Ahmad, O. Ahonen, M. Algaba, G. Alonso, V. Bergholm, R. Berwal, M. Beuerle, C. Bockstiegel, *et al.*, arXiv preprint arXiv:2408.12433 (2024).

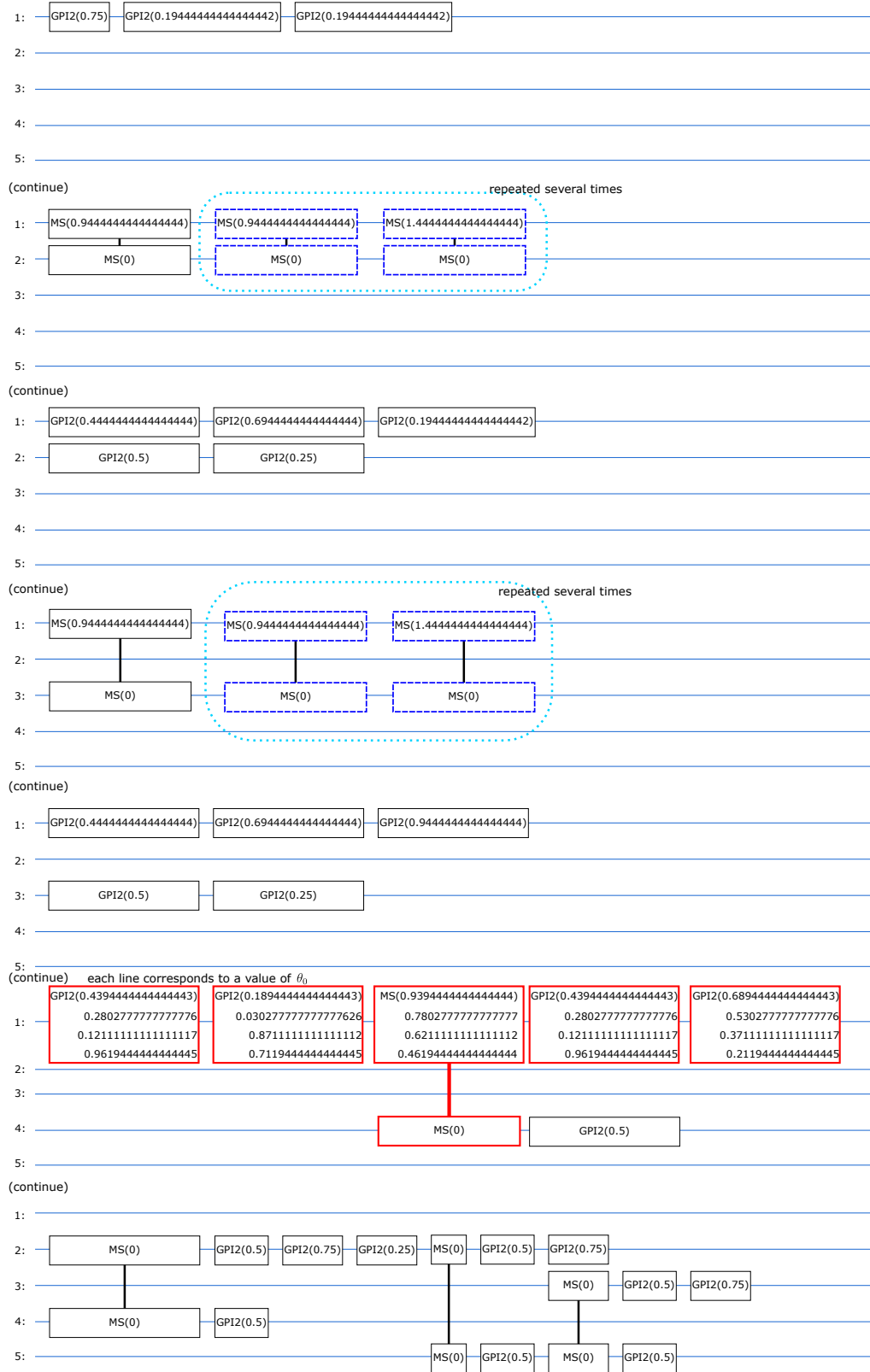


FIG. 5. The actual quantum circuits that were implemented on the IonQ Aria-1 quantum device. They correspond to the five-qubit syndrome measurement circuit (Fig. 2(a) in the main text). Redundant Mølmer-Sørensen gate pairs (corresponding to the identity channel in the ideal case) are inserted to tune the error rate. Note that the angles, after multiplied by  $2\pi$ , are in the unit of radius.